Journal of Solid State Chemistry **149,** 75–87 (2000)
Article ID jssc.1999.8498, available online at http://www.idealibrary.com on IDEAL®

CDW Superstructures in Hydrogen Molybdenum Bronzes H_xMoO_3

Stefan Adams

Mineralogisch-Kristallographisches Institut, Universität Göttingen, D37077 Göttingen, Germany

Received April 21, 1999; in revised form August 27, 1999; accepted September 7, 1999

Hydrogen molybdenum bronzes H_xMoO_3 ($0 < x < 2$) are consistently described as low-dimensional mixed conductors, whose properties under ambient conditions are controlled by charge density wave modulations. Proton conduction pathways in the bronzes are modeled by a bond valence approach. The redistribution of hydrogen during the intercalation process between two types of potential proton sites is simulated in a molecular mechanics study. Therefrom a structure model for the bronze phase II ($0.85 < x < 1.04$) is derived, which permits a Rietveld refinement of its previously unknown structure from powder X-ray data (space group $I12/m1$; $a = 14.5191(6)$ Å, $b = 3.7944(1)$ Å, $c = 7.7248(3)$ Å, $\beta = 93.743(2)^\circ$ for $x \approx 0.9$). Both the doubling of the host cell along the c-axis in phase II and the $6 \times c$ superstructure found for phase I with $x \approx 1/3$ meet the expectations for quasi-one-dimensional Peierls distorted systems. Modifications in the structure, proton ordering, and properties of the bronzes are studied as a function of temperature. A time-resolved powder XRD investigation on the oxidation of phase II indicates the existence of a intermediate phase $H_{0.6}MoO_3$. The powder structure determination of this metastable phase (space group $C2/m$, $a = 14.543(2)$ Å, $b = 3.8520(4)$ Å, $c = 3.7691(4)$ Å, $\beta = 90.73(1)^\circ$) indicates a redistribution of the protons during this oxidation step.

Key Words: **molybdenum bronze; charge density waves; Peierls transition; hydrogen intercalate.**

1. INTRODUCTION

The intercalation of hydrogen into the layered structure of orthorhombic MoO_3 produces five hydrogen molybdenum bronze phases H_xMoO_3 ($0 < x < 2$) (1–5). Technical applications of these low-dimensional mixed conductors as hydrogen transfer catalysts, electrodes in fuel cells, electrochromic devices, sensors, etc., require a detailed understanding of how their transport properties depend on host structure modifications, hydrogen distribution, and ordering among the two potential H^+ intercalation sites: channels within the MoO_3 layers or the van der Waals gaps (vdW gaps) between the layers (cf. Fig. 1). Besides recently reported spin glass states (6) and studies on charge density wave (CDW) states (7), which are the main topic of this work, a continued scientific interest in H_xMoO_3 phases is raised by the possibility of controlling the dimensionality of the transport processes via the hydrogen content and hence via the applied electric potential. Effects of the reduced dimensionality become the more important in low-dimensional samples such as the molybdenum bronze thin films used in electrochromic devices (8, 9). So far the complex interplay between CDW structure modulations and rearrangements of the mobile protons has limited the understanding of the hydrogen molybdenum bronzes when compared to the structurally related Magnéli phases Mo_nO_{3n-1} and alkali molybdenum bronzes (cf. (10, 11)).

2. EXPERIMENTAL

Powder samples of phase III were prepared by chemical reaction with "nascent" hydrogen following Glemser and coworkers (1, 2) and by electrochemical intercalation of hydrogen (12–14). Phase II powders were produced by the equilibration of phase III with the appropriate amount of MoO_3 following Birtill and Dickens (3). Thermochemical investigations have shown that this comproportionation is energetically favorable (15).

Single crystals of MoO_3 were grown by repeated sublimation of reagent grade MoO_3 powder. Homogeneous single crystals of phase I of up to $1.7 \times 0.8 \times 0.1\ mm^3$ were produced in the course of about 1 year by the modified spillover process described in (16). The reduction of phase I in the solid state electrochemical cell described in (16, 17) yielded crystals of higher hydrogen contents. With the help of these crystals it was possible to reveal the existence of a superstructures in phase III (7), but because of the minor quality of these crystals no single crystal structure determination has been attempted for the monoclinic phases.

The hydrogen content of the H_xMoO_3 powders was controlled by redox titrations (14, 18). The change in the hydrogen content of the molybdenum bronzes is reflected by variations in their lattice constants. Thereby approximate compositions for bronze phases in multiphase samples and for the single crystals were estimated from a determination

0022-4596/00 $35.00

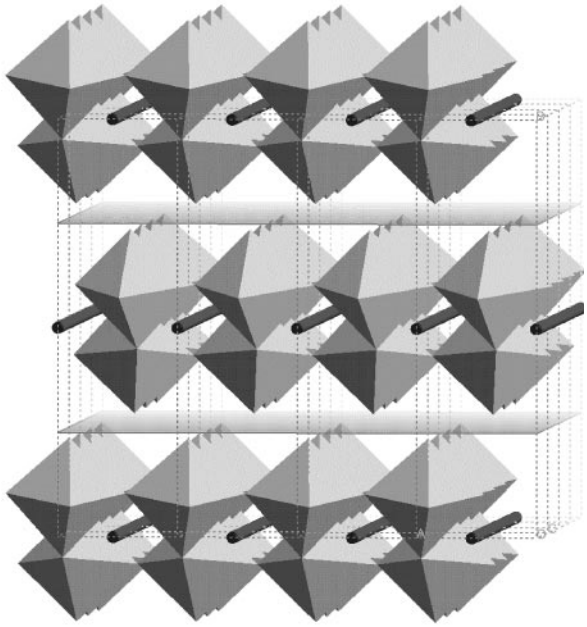

FIG. 1. Schematic view of the two types of potential H^+ intercalation sites in α-MoO_3: rods indicate the channels within the double-layers of MoO_6-octahedra; planes denote the "van der Waals gaps" between the layers.

of their lattice constants employing calibration curves from redox titrations of single phase powder samples. Within the homogeneity range of phase II our earlier calibration curves (7, 17) had to be adapted to the revised indexing of the powder patterns (see below).

Energy minimizations and molecular dynamics simulations have been performed utilizing the program Cerius2. Neutron single crystal data were taken at the D19 beamline of ILL Grenoble (19). X-ray single crystal data were taken on a Stoë four-circle diffractometer. Room temperature powder diffraction data were collected on a Philips PW1050 diffractometer, high-temperature powder XRD measurements employed an Anton Paar HTK high temperature camera on a Philips PW1820 diffractometer. All high temperature measurements were carried out in an inert atmosphere to reduce the loss of hydrogen during the experiment. In some of the samples the pronounced preferred orientation of the plate-like crystallites was reduced by the admixture of starch. This influenced the velocity of reoxidation under ambient conditions presumably by the increased amount of adsorbed water molecules. Rietveld-refinement with the program GSAS served for the determination of the lattice constants and in the case of new phases for the refinement of structure models obtained by molecular modeling. Single frequency ac conductivity measurements were performed with the Wayne Kerr bridge B905, impedance spectra were taken on a Solartron 1260 impedance analyzer.

3. RESULTS AND DISCUSSION

3.1. *Superstructure of $H_{0.3}MoO_3$*

Our earlier X-ray and conductivity study had revealed that the bronze phase I with the lowest hydrogen content (in the range $0.23 < x < 0.40$) undergoes a Peierls transition at $T_c \approx 380$ K (7). As the hydrogen positions could not be refined from the X-ray data at that time, valence bond calculations had been used to model the consequences of the Peierls distortion on the hydrogen distribution and ordering in the $3a \times \frac{2}{x}c$ superstructure (x = hydrogen content). All hydrogen atoms occupy channel sites forming hydrogen bonds between neighboring oxygen atoms. The CDW modulation causes an ordering of the protons into clusters of 6 OH groups, as shown schematically in Fig. 2. In the meanwhile such an investigation of displacive atomic modulation functions in CDW systems by the bond valence technique has been successfully applied to a variety of compounds (20). Owing to the limited size and quality of the available crystals it proved impossible to detect the superstructure reflections in a subsequent neutron single crystal study. A simultaneous refinement of neutron and X-ray data yielded results consistent to the previous X-ray study (19). In contrast to literature powder data our single crystal study confirmed IR data by Eda (21), that the asymmetry of Mo–O(2)–Mo bridges is diminished but not completely removed during the formation of phase I from MoO_3 (bond lengths 1.86 and 2.05 Å). Thus even the average structure at ambient temperature is only pseudoorthorhombic (space group $P2_1/b11$) (19).

No indications of a modulated phase had been found in two earlier neutron powder diffraction studies of

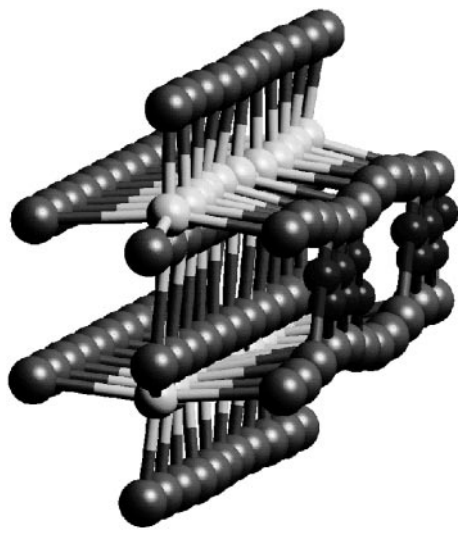

FIG. 2. Detail from the crystal structure of $H_{0.33}MoO_3$. The CDW modulation of the host lattice and the resulting localization of protons into clusters.

TABLE 1
Structure of $H_{0.28}MoO_3$ at 414 K

Atom	Site	x	y	z	n	U_{eq}/U_{iso}
Mo	*4c*	0.000	0.1035(7)	0.2500	1.0	0.018(3)
O(1)	*4c*	0.000	0.9331(8)	0.2500	1.0	0.012(3)
O(2)	*4c*	0.000	0.5859(8)	0.2500	1.0	0.017(3)
O(3)	*4c*	0.017(4)	0.2227(7)	0.2500	1.0	0.017(3)
H	*8f*	0.500	0.477(5)	0.529(2)	0.14	0.016(22)

Note. Space group, *Cmcm*; lattice constants: $a = 3.890(4)$ Å, $b = 14.18(1)$ Å, $c = 3.718(2)$ Å.

$D_{0.36}MoO_3$ (22) and $H_{0.31}MoO_3$ (23), where *Cmcm* was assigned as the space group at ambient temperature. Thus the first indications of a nonstatistic proton distribution within the channels originate from H NMR studies, which suggested 2 OH pairs (24), 3(OH) clusters (4), or a mixture of both (25). Larger clusters were neglected just because their spectra could not be simulated. With the progress in computational power the suggested cluster size increased and the most recent H NMR study (26) models the spectra of $H_{0.26}MoO_3$ by a superposition of contributions from n(OH) clusters with $n = 1$ to 6, suggesting that the main contribution is from 3–5(OH) clusters. This is well in line with the crystallographic result, since the 6(OH) clusters are not rigid units: the outer protons of the cluster may temporarily jump to adjacent sites within the channels splitting the cluster for short periods into subunits of variable size.

Our neutron single crystal structure determination of $H_{0.28}MoO_3$ in the disordered high temperature phase (19) yields atomic coordinates close to the room temperature values found by (22). All reflections that violate the extinction rules of space group *Cmcm* have vanished at $T = 414$ K. The proton intercalation sites remain unaffected by the phase transition, while the distortion of the Mo–O(2)–Mo bonds disappears (see Table 1).

3.2. Molecular Mechanics and Molecular Dynamics Modeling of the Intercalation Process

Starting from the force field parameter set UNIVERSAL by Rappé *et al.* (27), the force constants for MoO_3 including bond stretching, bond bending, Coulomb and van-der-Waals terms were adapted to fit the experimentally known pressure dependence of the lattice constants (28, 29). A simulation of the intercalation process must take into account that the intercalation is a redox reaction. Thus the force constants had to be continuously modified with the content of hydrogen, i.e., with the actual valence of the Mo atoms. At regular intervals during the simulation valences were calculated for the Mo and O atoms from an empirical bond length bond valence relationship (30). The effective Coulomb charge was then chosen as a constant fraction of the formal valence and force constants were adapted utilizing a relation between bond valence and force constant similar to the one proposed by Cotton and Wing (31). The preferred O–Mo–O bond angle equally depends on the bond valence, assuming a linear variation between the experimentally known boundary cases of 104° for Mo(VI) and 90° for Mo(IV) (32, 33).

In harmony with the structure determination of phase I (7, 22, 23) our molecular mechanics calculations indicate that the first intercalated H^+ form OH groups with the corner-sharing O atoms within the channels that extend along the *c*-direction. When the number of protons in these channels increases above 0.5, OH_2 groups must be formed. In a completely filled channel (i.e., for $x = 1$), the increased bond length between the Mo atoms and such OH_2 groups would result in insufficient distances between the corner-sharing O atoms, which is avoided by a gradual rotation of the OH_2 groups out of the channels into the vdW gap. Thereby the protons approach the terminal O atoms and form hydrogen bonds to them. At the same time the progressively reduced Mo valence favors a regular octahedral coordination driving the corner-sharing oxygen atom back into the octahedra layer. This is achieved by a flipping of the protons from the corner-sharing to the terminal O atoms, where again OH_2 groups are formed.

An ordered low energy configuration for the protons as OH_2 groups in the vdW gaps of H_1MoO_3 (obeying the ice rules) is possible only in a supercell of the host structure. This also implies an ordering of the MoO_6 octahedra that most likely occurs along the *c*-axis, for which neighboring octahedra share common edges. The simplest plausible structure proposal for ordered H_1MoO_3 is therefore a doubling of the *c*-axis.

We also tried to incorporate CDW structure modulations into our simulations by imposing fixed periodic modulations of the Mo valences. These calculations indicate that the boundaries of the composition ranges are determined by the mutual stabilization of proton ordering and charge density waves. The results are compatible with the suggestion of Ehses (34, 35) that even within the "homogeneity ranges" of the bronze phases not all compositions might be stable, but only a (large) number of commensurate states leading to an *incomplete devils staircase* of compositions.

Despite the choice of very simple boundary conditions (24 unit cells, NVT dynamics, apparent temperature $T = 300$ K), molecular dynamics simulations of the proton transport in phase I based on the above-mentioned force fields yielded realistic orders of magnitude for the proton diffusion coefficients in modulated LT- and HT-phase I. The CDW structure modulation in the low temperature phase decreases the $\log(D_{\|c}/\mathrm{cm}^2\ \mathrm{s}^{-1})$ from -6.0 to -7.8 along the channel direction c and the direction averaged value $\log(\langle D\rangle/\mathrm{cm}^2\ \mathrm{s}^{-1})$ from -6.4 to -8.2. Electrochemical determinations on LT-phase I single crystals accordingly

yielded $\log(D_{\|c}/\mathrm{cm}^2\ \mathrm{s}^{-1}) = -7.6$ (16, 36), while literature NMR data (4, 23, 24, 37) range from -7 to -9.7 mostly because of differing model assumptions.

A density functional study by Chen *et al.* (38) on the hydrogen adsorption at the (010) surface of α-MoO_3 confirms that the terminal oxygen atoms should be the most stable hydrogen binding sites for $x = 1$. Owing to the limited sizes of their model and the incorrectly assumed exclusive formation of OH groups the calculated binding energies can be taken only as a crude estimate.

3.3. *Superstructure Determination of Phase II ($H_{0.9}MoO_3$)*

Both H NMR studies by Ritter (4) and our electrochemical studies (16) indicate that the proton conductivity reaches a maximum for phase II ($0.85 < x < 1.04$). Based on an incomplete indexing of the XRD powder diagram Birtill and Dickens had suggested a similar unit cell as for $H_{1.6}MoO_3$ and the same space group $C2/m$ (3). So far no structure determination existed for phase II and various contradictory models for the hydrogen distribution and the transport mechanism were published. While Dickens *et al.* (22) suggested an exclusive occupation of the vdW gap for all monoclinic phases from their inelastic neutron scattering spectra, the increased lattice constant perpendicular to the layers was taken as evidence for a nearly complete occupation of intralayer channel sites by Ritter *et al.* (4). Similar arguments were used in subsequent modifications of Ritters approach by Bamberg and Schmitt (13, 39), as well as in our own earlier work (7). Tanaka *et al.* recently even concluded from their EXAFS and XANES spectra that instead of being an intercalate of α-MoO_3 the structure of $H_{0.91}MoO_3$ might rather be derived from rutile type MoO_2 (40).

Following Birtill and Dickens (3) several reflections that remained unindexed by their unit cell proposal were generally traced back to the formation of molybdenum suboxides such as Mo_8O_{23} and Mo_9O_{26}. On the other hand, thermogravimetric and DTA investigations demonstrate that the postulated evolution of H_2O from the bronze phases occurs only at higher temperatures for an inert atmosphere, while under mild conditions the deintercalation of hydrogen from the bronzes in the presence of oxygen and/or platinum (for the bronze samples produced by spillover) does not lead to oxygen deficient oxides (37, 41).

Our MD simulations suggested a doubling of the unit cell c with respect to the host structure, which subsequently proved to allow for a complete indexing of the powder diagram in space group $I12/m1$ (see Table 2). This nonstandard setting of space group $C2/m$ has been selected to produce the unit cell with the maximum similarity to the structures of the host MoO_3 and of the remaining hydrogen molybdenum bronze phases.

While Peierls distortions of quasi-one-dimensional solids generally give rise to incommensurate superstructures of periodicity $2/x$ times the undistorted lattice constant (where x denotes the number of transferred electrons $\approx$ number of intercalated protons per formula unit H_xMoO_3), commensurate superstructures are energetically preferable if $2/x$ approaches a rational number. The $2c$ superstructure thus meets the expected value for a Peierls distortion in the nearly half-filled Mo–O valence band.

Starting from models generated by our MD simulations the crystal structure of phase II was solved and refined including the H positions by Rietveld analysis of the X-ray powder data. Details of the refinement and positional parameters will be published elsewhere (42). The intercalated protons predominantly reside in the vdW gap forming OH_2 groups with the terminal oxygen atom of the MoO_6 octahedron around Mo(1). Following the electronically imposed superstructure these OH_2 groups are ordered into chains along the b-direction perpendicular the intralayer channels (Fig. 3). Thereby the observed fast proton transport cannot, as previously suggested (4), be explained by a collective transport mechanism within nearly filled channels, but occurs within the vdW gaps. The high mobility of the protons in the vdW gaps may then be understood by the large number of vacant proton sites, which are arranged in rows parallel to the occupied sites. From the X-ray data it cannot be ruled out that a small fraction of the protons might occupy channel sites in the vicinity of the $Mo(2)O_6$-octahedra, but as demonstrated further below the mobility of such protons would not contribute significantly to the long-range proton transport.

The assumption of a charge density wave superstructure is supported by the remarkable differences between the two crystallographically distinct MoO_6 entities shown in Fig. 4: the octahedron around Mo(1), to which the protons are attached, closely resembles the one reported for $H_{1.7}MoO_3$ (43, 44), while both bond lengths and bond angles around Mo(2) are similar to the ones in $H_{0.36}MoO_3$. Employing the empirical relation by Brown and Wu (30) the total valence of the Mo–O bonds can be assessed to be only 4.4 for Mo(1) compared to 5.5 for Mo(2). In harmony with the respective valence state, bond angles around Mo(1) are almost rectangular (88°), whereas for Mo(2) the average bond angle is about 101°. The agreement between the refined hydrogen positions and the host lattice distortion may also be expressed in terms of bond valence sums for the oxygen atoms, if only Mo–O bonds are considered. Then the bond valence of the terminal oxygen atom O(5) attached to Mo(1) is only 0.4, so that $\Delta V = 1.6$ bond valence units from bonds to hydrogen are needed to reach the formal oxygen valence of 2. Bond valence deviations $\Delta V \approx 0.2$ for the terminal O(6) atom at Mo(2) as well as for O(1) imply that a small number of protons may be bonded to these atoms, while the valence deviations for the remaining oxygen atoms are $< 3\%$.

Figure 5 illustrates the network of hydrogen bonds that interconnects adjacent layers. The asymmetry of this net-

TABLE 2
X-Ray Powder Data of Monoclinic $H_{0.9}MoO_3$

h	k	l	d_{obs} (Å)	d_{cal} (Å)	Int. (a.u.)	h	k	l	d_{obs} (Å)	d_{cal} (Å)	Int. (a.u.)
2	0	0	7.2418	7.2440	663	8	0	−2	1.6815	1.6819	59
1	**0**	**1**	**6.6240**	**6.6280**	**10**	7	1	−2	1.6815	1.6811	59
3	**0**	**−1**	**4.2164**	**4.2183**	**37**	**4**	**2**	**0**	**1.6815**	**1.6806**	**59**
3	**0**	**1**	**3.9767**	**3.9774**	**37**	2	2	−2	1.6673	1.6678	118
1	1	0	3.6704	3.6706	1000	**7**	**0**	**−3**	**1.6673**	**1.6658**	**118**
4	0	0	3.6185	3.6220	197	2	2	2	1.6462	1.6465	76
2	0	−2	3.4964	3.4986	307	**6**	**1**	**−3**	**1.6406**	**1.6409**	**30**
2	0	2	3.3111	3.3140	238	8	0	2	1.5988	1.5994	32
2	**1**	**1**	**3.0464**	**3.0474**	**18**	**8**	**1**	**1**	**1.5806**	**1.5801**	**38**
3	**1**	**0**	**2.9810**	**2.9836**	**7**	**5**	**2**	**−1**	**1.5657**	**1.5657**	**24**
5	**0**	**−1**	**2.7727**	**2.7726**	**75**	**4**	**2**	**−2**	**1.5573**	**1.5579**	**62**
4	0	−2	2.7287	2.7298	56	6	0	−4	1.5573	1.5566	62
1	1	−2	2.6791	2.6802	139	4	2	2	1.5236	1.5237	31
1	1	2	2.6345	2.6363	81	5	1	−4	1.5173	1.5171	18
4	0	2	2.5565	2.5574	75	6	2	0	1.4923	1.4918	78
4	**1**	**−1**	**2.5159**	**2.5171**	**47**	**6**	**0**	**4**	**1.4607**	**1.4604**	**19**
6	0	0	2.4149	2.4147	375	**5**	**1**	**4**	**1.4415**	**1.4415**	**12**
3	1	2	2.3137	2.3145	71	**8**	**1**	**−3**	**1.4177**	**1.4174**	**23**
5	1	0	2.3027	2.3029	117	**9**	**0**	**−3**	**1.4069**	**1.4061**	**5**
2	**1**	**−3**	**2.0709**	**2.0718**	**4**	**7**	**2**	**1**	**1.3655**	**1.3655**	**23**
5	**1**	**−2**	**2.0218**	**2.0237**	**4**	**0**	**2**	**4**	**1.3521**	**1.3515**	**73**
6	**1**	**−1**	**1.9972**	**1.9969**	**30**	**10**	**1**	**−1**	**1.3477**	**1.3472**	**36**
7	**0**	**1**	**1.9673**	**1.9670**	**50**	**5**	**2**	**3**	**1.3292**	**1.3293**	**9**
6	**1**	**1**	**1.9424**	**1.9433**	**35**	**2**	**2**	**4**	**1.3183**	**1.3182**	**16**
0	0	4	1.9264	1.9271	133	**8**	**2**	**0**	**1.3102**	**1.3100**	**10**
0	2	0	1.8971	1.8972	177	**4**	**2**	**−4**	**1.2860**	**1.2860**	**22**
2	**0**	**−4**	**1.8917**	**1.8933**	**46**	**7**	**1**	**4**	**1.2860**	**1.2857**	**22**
5	**0**	**3**	**1.8624**	**1.8630**	**13**	**2**	**0**	**−6**	**1.2795**	**1.2794**	**13**
2	2	0	1.8346	1.8353	65	**1**	**3**	**0**	**1.2600**	**1.2600**	**36**
7	**1**	**0**	**1.8172**	**1.8170**	**98**	**7**	**2**	**−3**	**1.2518**	**1.2518**	**19**
8	0	0	1.8111	1.8110	35	**8**	**2**	**2**	**1.2231**	**1.2228**	**16**
4	**1**	**3**	**1.7921**	**1.7926**	**12**	**1**	**1**	**−6**	**1.2190**	**1.2189**	**9**
4	0	−4	1.7491	1.7493	11	**6**	**2**	**−4**	**1.2031**	**1.2034**	**24**
1	1	−4	1.7179	1.7180	53	**9**	**2**	**1**	**1.2031**	**1.2029**	**24**
1	1	4	1.6944	1.6947	77	**1**	**3**	**−2**	**1.1995**	**1.1994**	**16**

Note. Miller indices that differ from those reported by Birtill and Dickens (except for the doubling in index l) are printed in bold. Space group, $I12/m1$ (= No. 12 $C2/m$); $a = 14.5191(6)$ Å, $b = 3.7944(1)$ Å, $c = 7.7248(3)$ Å, $\beta = 93.743(2)^\circ$.

work stabilizes the monoclinic angle β. The dominance of the electronic effect over the proton ordering is visualized by the observation that the refined H positions are not as commonly expected along the shorter O–O distances across the vdW gap. Due to ice rule restrictions an ordered occupation of those sites would permit the intercalation of 0.5 H per formula unit only for the given Mo charge ordering.

The observed H distribution bears a number of similarities to the one reported from a powder neutron diffraction study of phase III ($D_{1.65}MoO_3$), where about 0.8 H per formula unit were found to be localized in chains along the b direction (43). The two parallel rows of H positions found in a second neutron powder study on phase III ($D_{1.68}MoO_3$) differ considerably in their atomic displacement parameters, i.e., in their degree of localization (44). Similarly, Slade *et al.* suggested from their temperature dependent incoherent QENS study the existence of two slowly exchanging H-populations with a different degree of localization within the vdW gaps of $H_{1.68}MoO_3$ (45). None of these phase III powder studies reported any sign of a superstructure, so that the proton ordering could not be correlated to a Peierls distortion, whereas satellite reflections corresponding to a $2a \times 2c$ superstructure had been observed for phase III single crystals below the phase transiton at $T_c \approx 60^\circ$C (7).

A comparison of the incoherent inelastic neutron scattering (IINS) spectra of phases II and III reported in Refs. (22, 46) further substantiates our structure determination of phase II. The spectrum of $H_{0.93}MoO_3$ is more complex than that of phase III, but contains a prominent excitation

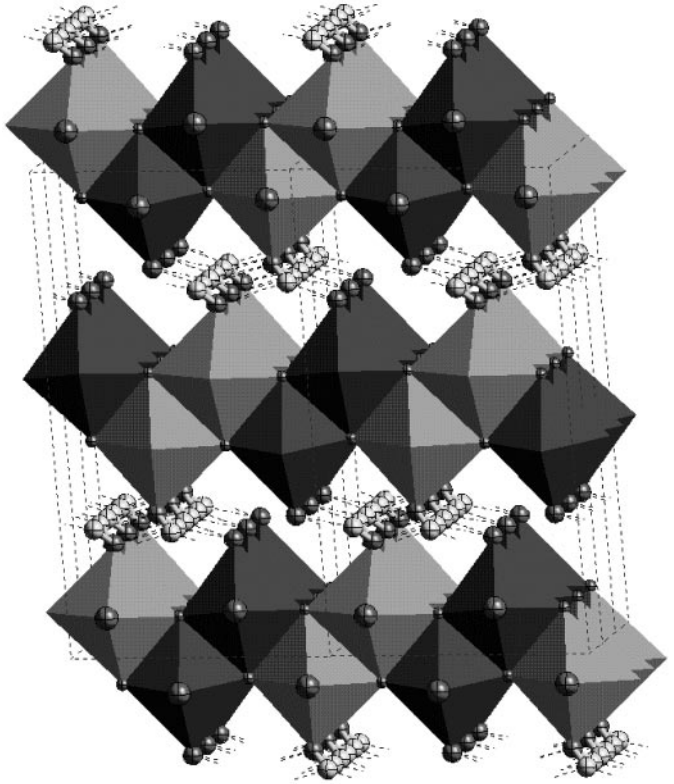

FIG. 3. Overview of the structure of $H_{0.9}MoO_3$ showing the two crystallographic different MoO_6 units (light and dark octahedra). Protons form OH_2 groups with the terminal O atoms of only one type of octahedra. The OH_2 groups are arranged into chains along the *b*-axis.

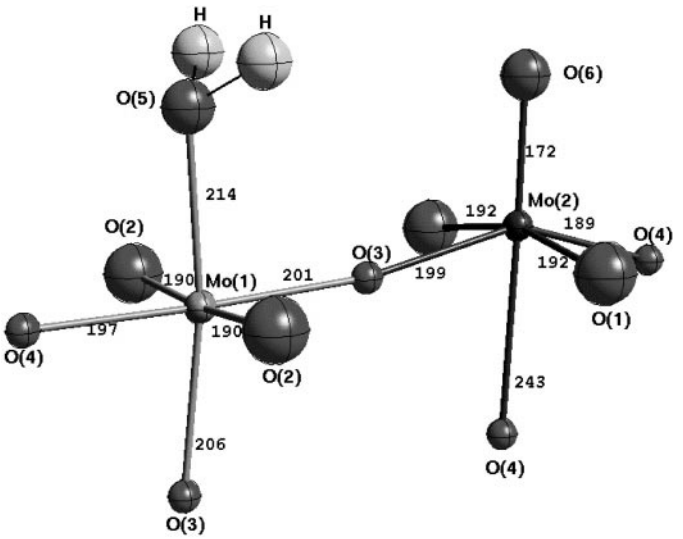

FIG. 4. Comparison of the Mo–O bond lengths within the two MoO_6 octahedra. The notable lengthening of the terminal Mo(1)–O(5) bond substantiates the refined H positions in the vicinity of O(5). Differences in the bond angles of Mo(1) and Mo(2) equally reflect the different charge densities.

at $\nu = 395\,\mathrm{cm}^{-1}$. Adopting the common assignment of a band at practically the same frequency in the IINS spectrum of phase III as originating from the stretching of the Mo–OH_2 bond and employing an empirical bond length–vibration frequency relation proposed by Hardcastle and Wachs (47), a Mo(1)–O(5) bond length of 2.13 Å is to be expected in perfect agreement with 2.14 Å found in the structure refinement. The identification of the Mo(2)–O(6) bond stretching frequency is less straightforward, but the band at $912\,\mathrm{cm}^{-1}$, which would correspond to a bond length of 1.73 Å, may be tentatively assumed. IINS (22), IR (21, 23, 48), and Raman (23, 48, 49) studies find $\nu \approx 1000\,\mathrm{cm}^{-1}$ for the somewhat shorter terminal Mo–O bonds in MoO_3 and phase I. No corresponding vibration frequency is observed in the spectra of phase III. Slight changes in the Raman spectra of MoO_3 implanted with protons (50) might indicate the formation of (oxygen) defects rather than the formation of a hydrogen bronze.

3.4. Proton Transport Pathways

Bond length bond valence calculations are not only meaningful in localizing the protons in the hydrogen molybdenum bronzes. They also provide a simple and vivid tool for the study of the ionic transport (see, e.g., (51, 52)). For this purpose connections between H^+ equilibrium sites, along which the required deviation from the ideal valence sum V for the H remains as small as possible are taken as probable transport pathways, while the extent of the required valence mismatch ΔV to produce an infinite pathway should be linked to the activation energy for the dc ionic conductivity. The differences between the proton transport

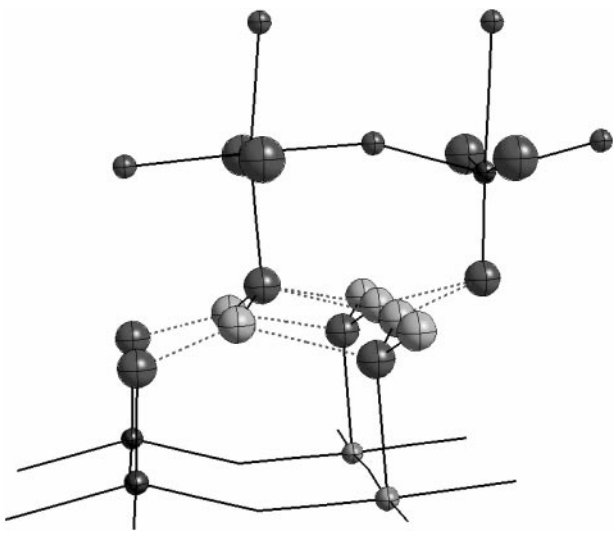

FIG. 5. Adjacent layers of octahedra are linked by a network of hydrogen bonds, which stabilizes the monoclinic angle.

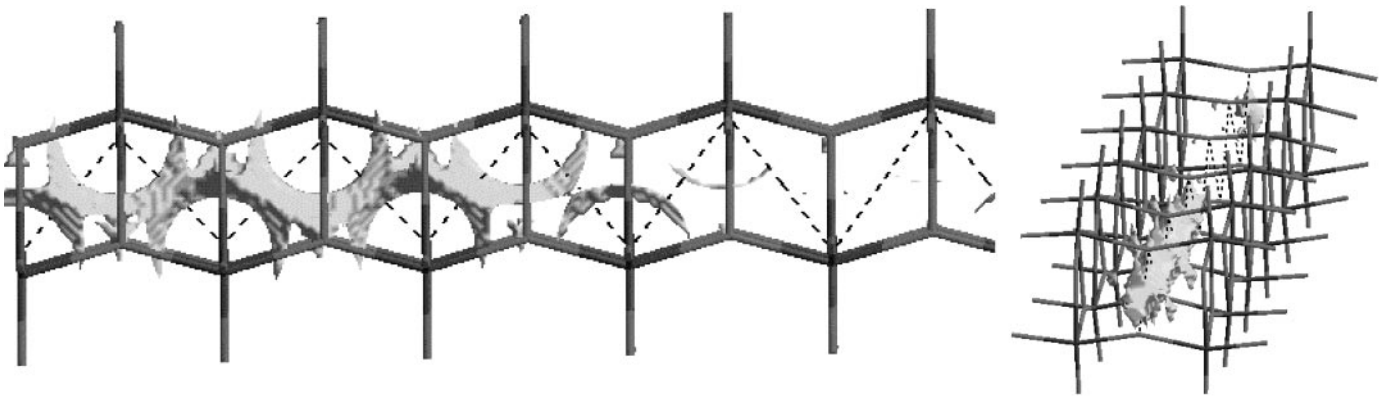

FIG. 6. Bond valence model for the mobility of protons within one channel of the CDW modulated phase I. The valence mismatch isosurface encloses regions where the valence for a H deviates up to 0.25 from the equilibrium value $V = 1$. At this level the motion of protons remains restricted to the vicinity of the cluster sites, while a long-range conductivity would require a higher activation energy.

pathways in the modulated phases I and II are displayed in Figs. 6 and 7. There the three-dimensional hydrogen valence mismatch isosurfaces enclose the accessible volume for the H^+. The valence map of phase I highlights the effective localization of the protons into clusters of OH groups. The respective valence isosurface for the same valence mismatch in the undistorted high-temperature phase yields a continuous pathway including channel H^+ sites.

Within phase II the H^+ transport pathway of lowest energy connects the chains of almost fully occupied sites in the vdW gaps. A slightly higher value of the valence mismatch incorporates the parallel rows of vacant proton sites into this pathway. From the side view of the isosurface it can be seen that a minor fraction of the protons might still reside in the intralayer channels, but they cannot contribute to a long-range ionic transport, since their motion would be restricted to local hops among the neighboring channel sites.

3.5. Characterization of Phase II

Various peculiarities of the conductivity in phase I were compiled in Refs. (7, 14, 16) in order to verify the CDW nature of the modulated state. Besides the direct observation of the Peierls transition, this included voltage oscillations, the significant field dependence of the conductivity in

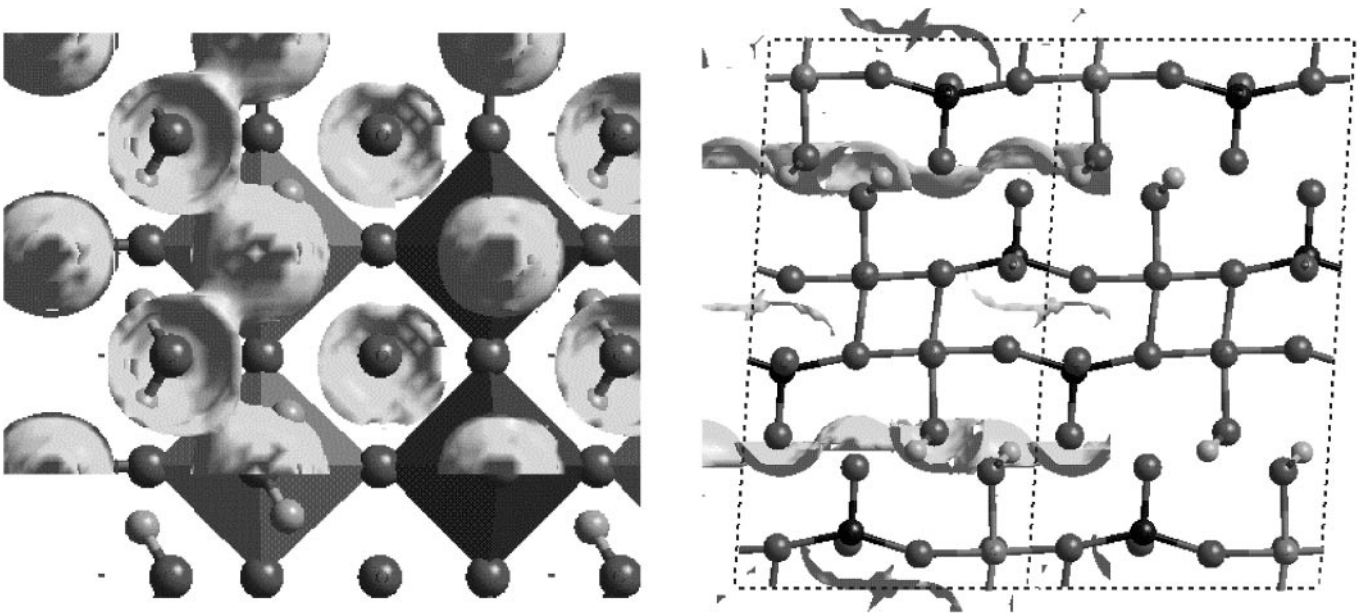

FIG. 7. Top and side view of a bond valence model for the mobility of protons within the CDW modulated phase II. The infinite pathway that requires the lowest bond valence mismatch occurs within the van der Waals gap, while potential H sites within the channels remain localized.

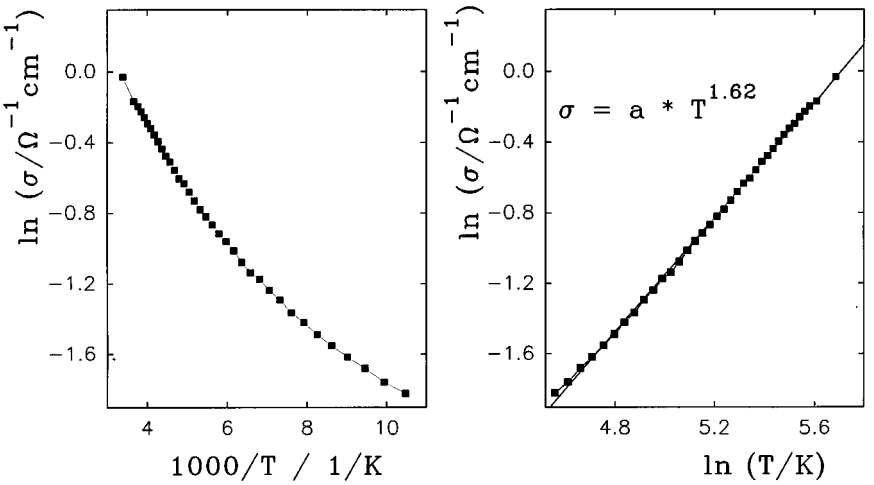

FIG. 8. The temperature dependence of the electric conductivity for a powder sample of phase II exhibits a pronounced deviation from an Arrhenius type behavior (left). The $\ln\sigma$–$\ln T$ plot (right) demonstrates that this subactivated behavior may be characterized by a power law.

the Peierls distorted state indicating a conductivity contribution from a collective motion of the depinned CDW (Fröhlich conductivity) as well as the characteristic deviation of conductivity from the Arrhenius type temperature dependence of normal semiconductors.

No such detailed conductivity study could be performed for phase II because of the low stability of this bronze phase in contact to metallic electrodes especially at elevated temperatures. Still the characteristic non-Arrhenius type temperature dependence has been observed in the temperature dependence of the specific conductivity $\sigma(T)$ of phase II powder samples below room temperature (Fig. 8). A more appropriate description for the temperature range 100–300 K is achieved by the power law

$$\sigma \propto T^{1.6}$$

Conductivity measurements of a phase II single crystal along the *c*-direction in the same temperature range indicate a stronger temperature dependence along the CDW modulated "nesting direction," yielding $\sigma \propto T^{4.1}$ (36). This might be somewhat biased by an inhomogeneity of the crystal, but nevertheless provides a crude estimate for the anisotropy of the band gap (cf. the anisotropy of the band gap in η-Mo_4O_{11} (53)).

This type of subactivated behavior, which is known for a variety of quasi-one-dimensional CDW systems (see, e.g., (54–56)), is generally attributed to electron-hopping processes between bound solitons. With decreasing temperature the contribution of this hopping process to the total conductivity becomes more and more important (56, 57).

While the catalyzing effect of metal electrodes on the evolution of hydrogen impedes reliable conductivity measurements at higher temperatures, the existence of a phase transition is observable from the shift of Bragg peak positions in high temperature powder diffraction data (Figs. 9 and 10). The temperature dependence of the lattice constants for $H_{0.86}MoO_3$ as determined from Rietveld refinements with constant atomic parameters is summarized in Fig. 11.

A slight loss of hydrogen proved to be inevitable during the heating experiment. Since the lower limit of the homogeneity range of phase II was chosen as the initial composition of the sample, this resulted in the partial transformation to a second monoclinic phase of slightly reduced hydrogen content. Rietveld refinement permitted the simultaneous refinement of the lattice constants for both phases. Results for the second phase are discussed further below. For phase II, a phase transition at $T \approx 95°C$ is clearly seen from the variation of the monoclinic angle and of the lattice constants *b* and *c*, whereas the change in the thermal expansion

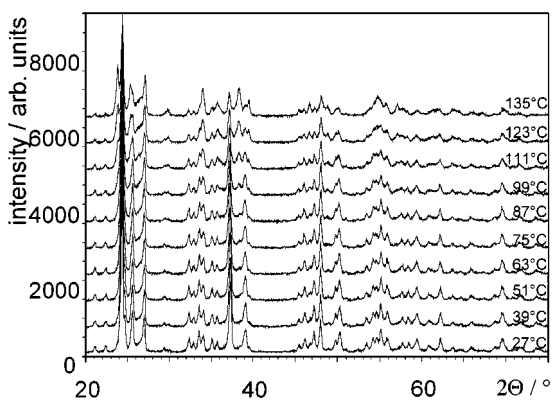

FIG. 9. Detail from the high-temperature powder diffractograms of phase II in the temperature range from 27 to 135°C.

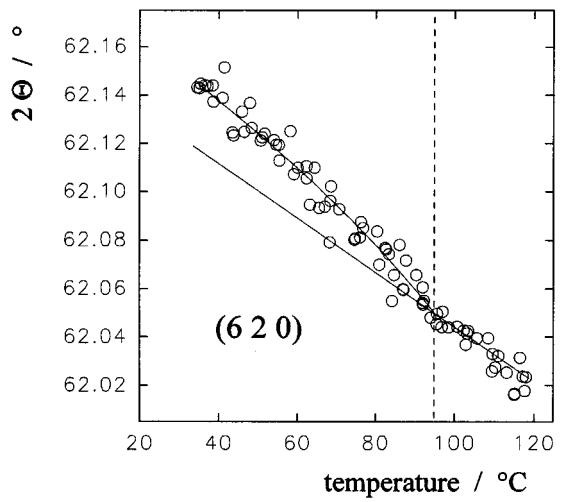

FIG. 10. Temperature dependence of Bragg angle 2Θ for the (620) peak of $H_{0.9}MoO_3$, indicating a phase transition at $T \approx 95°C$.

along the *a*-axis remains rather small. Thus it may be concluded that the transition affects the CDW modulation along *c* and thereby also the ordering of protons within the vdW gaps, but does not cause an increased occupancy of the intralayer channels which should be related to a substantial change in the lattice expansion perpendicular to the layers. This behavior deviates from our observations for the corresponding phase transition at $T \approx 60°C$ in $H_{1.6}MoO_3$, where the spontaneous deformation indicates a change in the hydrogen distribution between channels and vdW gaps (7).

Bragg peaks that correspond to the superstructure of phase II do not vanish at this transition temperature, but the peaks broaden and their intensity decreases significantly. At about 180°C the superstructure reflections have completely vanished (Fig. 12). Due to the limited stability of the samples at high temperatures it remained unclear, whether this second transition temperature depends on the heating rate. It appears plausible, that the modulated structure with an ordered arrangement of OH_2 groups persists as a metastable phase above the Peierls transition.

A similar decoupling of Peierls transition and proton ordering had also been supposed from conductivity data in phase I (7, 34, 35). Analoguous diffuse spots, which have been observed for single crystals of various CDW systems in the temperature range above T_c, are accordingly ascribed to metastable medium-range correlations between structure modulations (58).

3.6. *Formation of Metastable $H_{0.6}MoO_3$ (Phase IIa)*

Under ambient conditions (undried air atmosphere, $T = 20°C$) phase II is slowly oxidized to $H_{0.4}MoO_3$. *In situ* powder XRD studies display that the first step of this reaction is the formation of $H_{0.6}MoO_3$ within roughly 400 h (see Fig. 13). After a total reaction time of 1500 h the samples were transformed into $H_{0.4}MoO_3$. A complete conversion of phase II into $H_{0.6}MoO_3$ was observed only in samples that contained an admixture of starch to reduce the preferred orientation of the plate-like crystallites. Both water molecules adsorbed by the starch and the reduced contact between bronze crystallites might affect the rate determining step of the hydrogen transfer. The powder pattern of $H_{0.6}MoO_3$ was indexed based on space group $C2/m$ and a unit cell with $a = 14.543(2)$ Å, $b = 3.8520(4)$ Å, $c = 3.7691(4)$ Å, $\beta = 90.73(1)°$. The name "phase IIa" has been selected for this phase in order to retain the established numbering of the hydrogen molybdenum bronze phases and to emphasize the close structural relation of the additional phase to phase II with $x \approx 1$. The crystal structure of phase IIa has been solved from X-ray powder data (29). The results of the subsequent Rietveld refinement (Fig. 14) are summarized in Table 3.

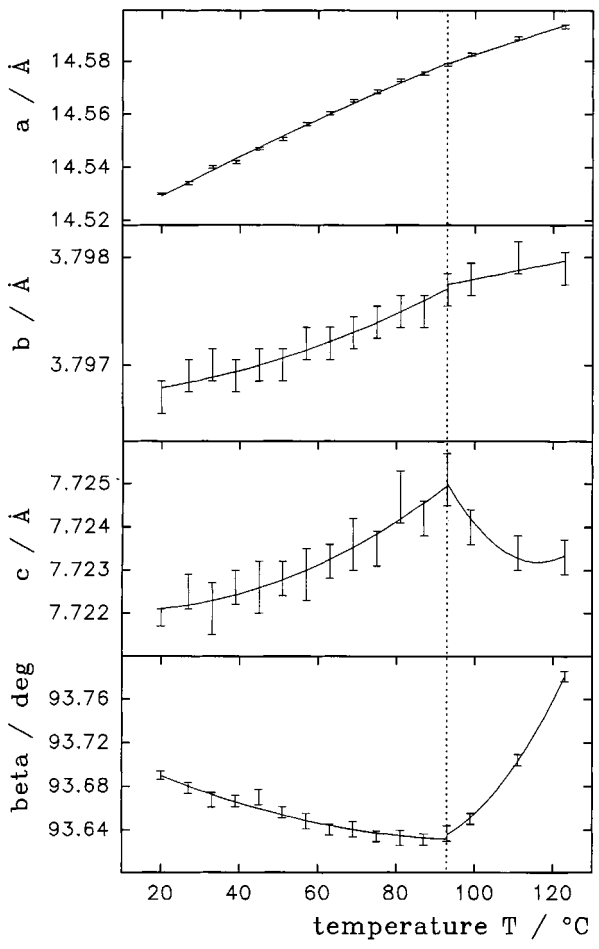

FIG. 11. Thermal expansion of $H_{0.86}MoO_3$. The sign of the temperature dependence changes at the transition temperature $T_c \approx 95°C$ both for the lattice constant *c* and for the monoclinic angle β.

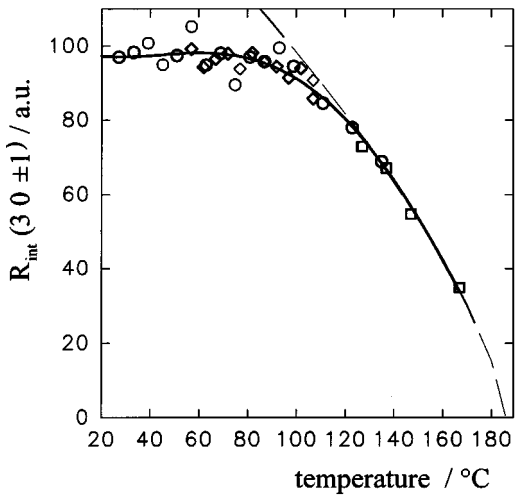

FIG. 12. Temperature dependence of the integrated intensity for the Bragg peaks (3 0 1) and (3 0 $\bar{1}$) of the modulated phase II.

The main difference between the powder diagrams of phases IIa and II is the vanishing of the superstructure reflections indicating that there is no more long-range charge and proton ordering. Valence sum calculations yielding the largest deviation from $V = 2$ for the oxygen atom O(2) indicate that the loss of H^+ ordering in $H_{0.6}MoO_3$ is associated to a proton transfer from the vdW gap into the "channel positions," which are exclusively occupied in the final oxidation product phase I. Indeed a potential proton site has been found in a difference Fourier synthesis at a reasonable distance from O(2). Although the H position was stable on refinement, it should be understood only as evidence for the occupation of the channels, while the refined position might be an average of several unresolved H sites. The occupation factor of the hydrogen site was finally fixed to the total hydrogen content ($n = 0.6$) since it tended to increase above this value.

The hydrogen bond network, which stabilized the monoclinic angle in phase II, is at least weakened in phase IIa by the reduced occupation of the vdW gaps. Consequently the monoclinic angle approaches 90° and the terminal oxygen atom is characterized by strongly anisotropic atomic displacement parameters and/or a significant static disorder (the latter was assumed in the Rietveld refinement).

The occurrence of an intermediate H_xMoO_3 phase with a hydrogen content of roughly $0.6 < x < 0.8$ during the reoxidation of phase II had been detected earlier by Schöllhorn and co-workers from the potential variation during an electrochemical oxidation experiment (5, 59). We assume that the phases are the same, although the lattice constants reported in (59) ($a = 14.631$ Å, $b = 3.8416$ Å, $c = 3.7675$ Å, $\beta = 90.73°$ for $x = 0.6$ and $a = 14.657$ Å, $b = 3.8424$ Å, $c = 3.7692$ Å, $\beta = 90.78°$ for $x = 0.8$) agree only qualitatively with our findings. A cointercalation of water into this bronze phase can be excluded because the intercalation of a water molecule would require a considerably larger interlayer spacing (cf. the lattice constants for a crystal of approximate composition $H_{0.25}(H_2O)_{0.5}MoO_3$: $a = 18.79$ Å, $b = 3.746$ Å, $c = 3.864$ Å, $\beta = 92.4°$ (17) and the interlayer distance $a/2 = 9.31$ Å reported by (60) for "$H_{0.5}(H_2O)_yMoO_3$").

Figure 16 displays the temperature-dependent variation of the lattice constants for phase IIa, as determined by Rietveld refinement for a sample containing mainly phase II. Therefore the hydrogen content of phase IIa may be estimated to be $x \approx 0.8$ according to Ref. (59). As only a minor fraction of the sample existed in phase IIa, the resulting lattice constants are considerably less precise than for the major phase II (cf. Fig. 11). Nevertheless, a comparison of the thermal expansion for the two phases reveals pronounced differences. The thermal expansion along the *a*-axis (perpendicular to the layers) is about five times higher in phase IIa, which harmonizes with the smaller number of hydrogen bonds between the layers. The negative thermal expansion along the *b*-axis might then be tentatively traced

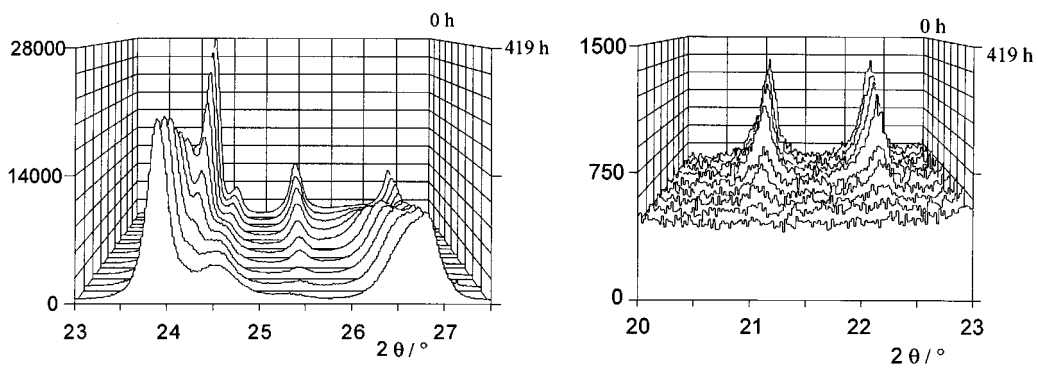

FIG. 13. Intensity variation of several main Bragg peaks (left) and of the two superstructure reflections (3 0 ±1) (right) as a function of time during the oxidation of a phase II powder.

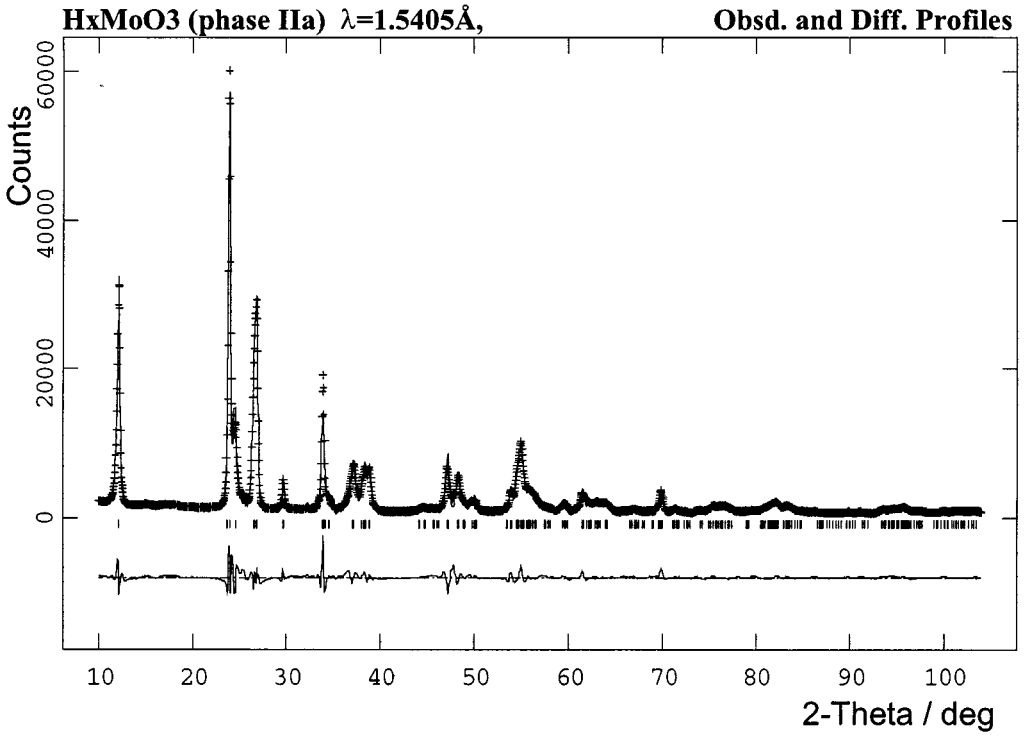

FIG. 14. Rietveld refinement of the metastable H_xMoO_3 phase IIa ($x \approx 0.6$).

back to a rearrangement of protons from the channel sites to the interlayer sites at higher temperatures. Still, such an interpretation of lattice constant variations should only be taken as a working hypothesis.

Rüschendorf (59) found it impossible to produce phase IIa by a comproportionation of phase III with MoO_3, supposing that (in contrast to the previously known hydrogen molybdenum bronzes) phase IIa should be metastable. Due to the low thermal stability of phase IIa and the admixture of other phases (starch, water) in our samples, it was not possible to determine the hydrogen content of this bronze precisely. The results of our redox titrations for homogeneous samples ($x = 0.6$–0.7) lay within the homogeneity range proposed by (5, 59).

Recently Eda *et al.* (6) independently found a new monoclinic H_xMoO_3 phase with $0.25 < x < 0.45$ during the reoxidation of phase III powder samples. According to data read from their lattice-constants-vs-hydrogen-content diagram ($a \approx 14.44$–14.67 Å, $b \approx 3.87$–3.84 Å, $c \approx 3.74$–3.78 Å, $\beta = 90.4$–91°), this phase is presumably identical with Schöllhorn's phase. While slightly different compositions for differently prepared samples may in general be traced back to the well-known hysteresis effect in such low-temperature solid state reactions (see, e.g., (5, 61)), in this case the strong deviation might also reflect the difficulties of an accurate hydrogen content determination for these phases. In this context it should be noted that the hydrogen contents reported in (6) for phases I, II, and III also lie considerably below the commonly accepted values of Birtill and Dickens (3). *In situ* XRD investigations of pure molybdenum bronzes as well as of stabilized composite samples (62) under a controlled electrical potential are presently in progress to improve the accuracy of the lattice constants vs hydrogen content calibration curves.

4. CONCLUDING REMARKS

The combination of a time resolved XRD study of the oxidation with MD simulations yields a revised model of the interplay between changes in structure and transport properties during intercalation. Distribution, ordering, and dynamics of the protons are dominated by changes in the electronic state of the host. Stable hydrogen bronze phases occur if the H^+ ordering is compatible to the CDW superstructure.

In the case of the modulated phase II the Peierls instability favors a multiplication of the cell constant c by a factor of $2/x$. Since x is close to 1 the energy gain by commensurability gives rise to a commensurate $2c$ superstructure, the textbook example of Peierls transitions. For phase I the commensurate models with cell multiplications of 6–7 along the c axis (7, 19) should rather be understood as simplifying models of the incommensurate superstructures.

TABLE 3
Details of the structure Refinement for Phase IIa at 293(2) K, Refined Structure Parameters, Selected Bond Lengths (Å) and Bond Valences

Composition	$H_{0.6}MoO_3$	Observed peaks	316
Formula weight	144.54 g/mol	Atoms	5
Color	Dark blue	Space group	$C2/m$
Wavelength	Cu$K\alpha$	R(wP)	0.118
2Θ range (°)	10–104	R(P)	0.088
Step size (°2Θ)	0.02	$R(F^2)$	0.048

$a = 14.543(2)$ Å, $b = 3.8520(4)$ Å, $c = 3.7691(4)$ Å, $\beta = 90.73(1)°$, $V = 211.13(4)$ Å^3

Atom	Site	x	y	z	n	U_{eq}/U_{iso}
Mo	*4i*	0.0967(2)	0	0.256(1)	1.0	0.033(2)
O(1)	*4i*	0.9312(8)	0	0.276(8)	1.0	0.027(1)
O(2)	*4i*	0.5824(7)	0	0.244(9)	1.0	0.029(5)
O(3)	*8j*	0.2090(10)	0.086(4)	0.186(7)	0.5	0.017(1)
H	*4i*	0.52(3)	0	0.28(6)	0.6	0.029[a]

Bond	Bond length (Å)	Bond valence after (30)
Mo–O(1)	1.813 2.043 2.409	2.09
Mo–O(2)	1.938 × 2	1.679
Mo–O(3)	1.691	1.898
O(2)–H	0.92	

[a] Constrained to the value for O(2).

The predictive power of the modeling techniques applied in this work is presently investigated by structural work on the quasi-two-dimensional hydrogen molybdenum bronze phases IV (the structure of which is not yet solved) and III, where present structure determinations neglect the observed superstructure.

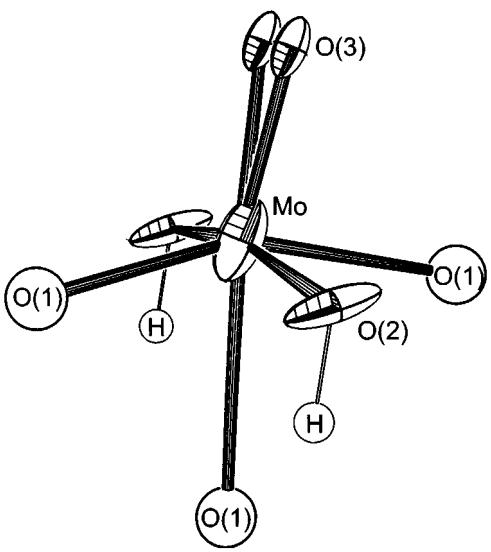

FIG. 15. MoO_6 octahedron of phase IIa as determined by the Rietveld refinement in Fig. 14.

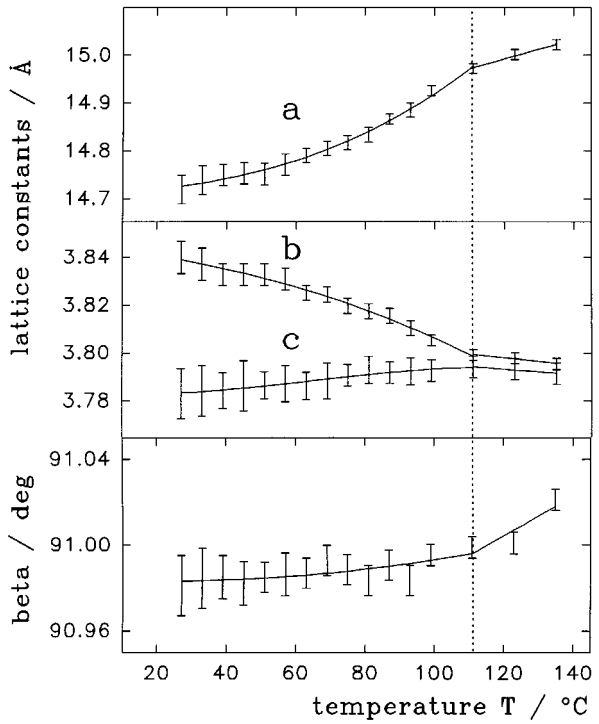

FIG. 16. Thermal expansion of phase IIa ($x \approx 0.8$) in a powder sample containing predominantly phase II.

The stabilizing effect of the proton ordering is visualized by the observation of slightly different transition temperatures for the Peierls transition and the proton ordering. When the Peierls distortion vanishes the ordered proton arrangement remains a local energy minimum and the ordered phase is metastable.

ACKNOWLEDGMENTS

Special thanks are due to Dr. Schönherr (MPI FKF Stuttgart) for growing single crystals of MoO_3 and to G. McIntyre (ILL Grenoble) for his kind support during the neutron single crystal measurements of $H_{0.3}MoO_3$. Helpful discussions with K. H. Ehses, P. G. Dickens, and K. Eda, as well as financial support from the Deutsche Forschungsgemeinschaft are gratefully acknowledged.

REFERENCES

1. O. Glemser and G. Lutz, *Z. Anorg. Allg. Chemie* **264**, 17 (1951).
2. O. Glemser, U. Hauschild, and G. Lutz, *Z. Anorg. Allg. Chemie* **269,** 93 (1952).
3. J. J. Birtill and P. G. Dickens, *Mater Res. Bull.* **13,** 311 (1978).
4. C. Ritter, W. Müller-Warmuth, and R. Schöllhorn, *J. Chem. Phys.* **83,** 6130 (1950).

5. R. Schöllhorn, *in* "Chemical Reactions in Organic and Inorganic Constrained Systems" (R. Setton, ed.), p. 323. Reidel, Dordrecht, 1986.
6. K. Eda, A. Sukejima, N. Matsuura, and N. Sotani, *Chem. Lett*. **1998,** 819.
7. St. Adams, K. H. Ehses, and J. Spilker, *Acta Crystallogr. B* **49,** 958 (1993).
8. C. Fukushima, M. Nagano, T. Sumita, H. Kubota, M. Nagata, Y. Honda, T. Oku, and J. Imahori, *Physica B* **239,** 56 (1997).
9. A. Guerfi, R. W. Paynter, and L. H. Dao, *J. Electrochem. Soc*. **142,** 3457 (1995).
10. J. Dumas and C. Schlenker, *Int. J. Mod. Phys. B* **7,** 4045 (1993).
11. M. Greenblatt, *Chem. Rev*. **88,** 31 (1988).
12. R. Schöllhorn, *Angew. Chem*. **92,** 1015 (1980), *Angew. Chem., Int. Ed. Engl*. **19,** 983 (1980).
13. J. Bamberg, *Thesis*. Saarbrücken, 1987.
14. G. Schwitzgebel and St. Adams, *Ber. Bunsenges. Phys. Chem*. **92,** 1426 (1988).
15. J. J. Birtill and P.G. Dickens, *J. Solid State Chem*. **29,** 367 (1979).
16. St. Adams, K. H. Ehses, and G. Schwitzgebel, *Synth. Met*. **43,** 3953–3956 (1991).
17. St. Adams, *Thesis*. Saarbrücken, 1991.
18. C. Choain and F. Marion, *Bull. Soc. Chim. Fr*. **1963,** 212.
19. St. Adams and G. McIntyre, ILL Experimental Report 5-15-402, 1995.
20. R. L. Withers, S. Schmid, and J. G. Thompson, *Prog. Solid State Chem*. **26,** 1 (1998).
21. K. Eda, *J. Solid State Chem*. **83,** 185 (1989).
22. P. G. Dickens, J. J. Birtill, and C. J. Wright, *J. Solid State Chem*. **28,** 185 (1979).
23. F. A. Schröder and H. Weitzel, *Z. Anorg. Allg. Chem*. **435,** 247 (1977).
24. R. C. T. Slade, T. K. Halstead, and P. G. Dickens, *J. Solid State Chem*. **34,** 183 (1980).
25. M. Kunimoto, K. Eda, N. Sotani, and M. Kaburagi, *J. Solid State Chem*. **99,** 395 (1992).
26. K. Eda, N. Sotani, M. Kunimoto, and M. Kaburagi, *J. Solid State Chem*. **141,** 255 (1998).
27. A. K. Rappé, C. J. Casewit, K. S. Colwell, W. A. Goddard, and W. M. Skiff, *J. Am. Chem. Soc*. **114,** 10024 (1992).
28. S. Åsbrink, L. Kihlborg, and M. J. Malinowski, *Appl. Crystallogr* **21,** 960 (1988), and **22,** 380 (1989).
29. St. Adams, "Proceedings, First International Conference on Inorganic Materials," E108. Versailles, 1998.
30. I. D. Brown and K. K. Wu, *Acta Crystallogr. B* **32,** 1957 (1976).
31. F. A. Cotton and R. M. Wing, *Inorg. Chem*. **4,** 867 (1965).
32. L. Kihlborg, *Acta Chem. Scand*. **13,** 954 (1959).
33. A. Magnéli, *J. Inorg. Nucl. Chem*. **2,** 330 (1956).
34. K. H. Ehses, St. Adams, S. Heusing, and G. Schwitzgebel, *DFG-Mitteilung* **22,** 107 (1995).
35. K. H. Ehses, *priv. commun*.
36. S. Heusing, diploma thesis, Saarbrücken, 1990.
37. N. Sotani, K. Eda, M. Kunimoto, *J. Chem. Soc. Faraday Trans*. **86,** 1583 (1990).
38. M. Chen, U. V. Waghmare, C. M. Friend, and E. Kaxiras, *J. Chem. Phys*. **109,** 6854 (1998).
39. J. Bamberg and H. Schmitt, *Solid State Ionics* **26,** 303 (1988).
40. T. Tanaka, H. Aritani, S. Yoshida, K. Eda, N. Sotani, and S. Hasegawa, *J. Phys. IV France* **7,** C2-1143 (1997).
41. N. Sotani, K. Eda, M. Sadamatu, and S. Takagi, *Bull. Chem. Soc. Jpn*. **62,** 903 (1989).
42. St. Adams, *in preparation*.
43. M. Anne, D. Fruchart, S. Derdour, and D. Tinet, *J. Phys. France* **49,** 505 (1988) and **49,** 1315 (1988).
44. P. G. Dickens, A. T. Short, and S. Crouch-Baker, *Solid State Ionics* **28–30,** 1294 (1988).
45. R. C. T. Slade, P. Hirst, B. C. West, R. C. Ward, and A. Magerl, *Chem. Phys. Lett*. **155,** 305 (1989).
46. A. V. Powell, M. J. Pointon, and P. G. Dickens, *J. Solid State Chem*. **113,** 109 (1994).
47. F. D. Hardcastle and I. E. Wachs, *J. Raman Spectrosc*. **21,** 683 (1990).
48. L. Seguin, M. Figlarz, R. Cavagnat, and J.-C. Lassègues, *Spectrochim. Acta A* **51,** 1323 (1995).
49. K. Eda, *J. Solid State Chem*. **98,** 350 (1992).
50. T. Hirata, K. Ishioka, and M. Kitajima, *Appl. Phys. Lett*. **68,** 458 (1998).
51. St. Adams and J. Maier, *Solid State Ionics* **105,** 67 (1998).
52. St. Adams, *Solid State Ionics*, Submitted for publication.
53. J. P. Sorbier, H. Tortel, A. Fournel, I. Oujia, *J. Phys IV France* **3,** C2-259 (1993).
54. S. Kivelson, *Phys. Rev. B* **25,** 3798 (1982).
55. C. Berthier, A. Jánossy, P. Butaud, and P. Segransan, *in* "Nuclear spectroscopy on Charge Density Wave Systems" (T. Butz, Ed.), p. 177. Kluwer, Dordrecht, 1992.
56. R. H. Friend, "Solitons and Condensed Matter Physics" (A. R. Bishop and T. Schneider, Eds.), Vol. 8, p. 199. Springer, Berlin, 1978.
57. W. P. Su, J. R. Schrieffer, and A. J. Heeger, *Phys. Rev. B* **22,** 2099 (1980).
58. J. P. Pouget *in* "Low-Dimensional Electronic Properties of Molybdenum Bronzes and Oxides" (C. Schlenker, Ed.), p. 87. Kluwer, Dordrecht, 1989.
59. F. Rüschendorf, Thesis. TU, Berlin, 1990.
60. R. Schöllhorn, R. Kuhlmann, and J. Besenhard, *Mat. Res. Bull*. **11,** 83 (1979).
61. J. Rouxel and M. Tournoux, *Solid State Ionics* **84,** 141 (1996).
62. F. Endres and G. Schwitzgebel, *J. Electroanal. Chem*. **415,** 23 (1996).